J Mater Sci (2006) 41:7571–7579
DOI 10.1007/s10853-006-0843-8

Fluorescence spectroscopy analysis of Al–Al_2O_3 composites with coarse interpenetrating networks

Robert J. Moon · Mark Hoffman · Shigemi Tochino · Chang Joo Lee · Giuseppe Pezzotti

Received: 24 October 2004 / Accepted: 9 November 2005 / Published online: 20 October 2006

Abstract Fluorescence microprobe spectroscopy was used to characterize the stress fields that develop within an interpenetrating Al–Al_2O_3 composite resulting from both the thermal expansion mismatch during sample processing, and from an external applied load. The 30 vol% Al–70 vol% Al_2O_3 composite that was investigated had an aluminum and alumina phase feature size of 50–100 μm. The residual thermal compressive stress measured in the alumina was ~40–340 MPa. The effect of varying the metal ligament size on the residual stress distribution is discussed. Additionally, the application of an external load caused a non-uniform stress distribution to develop within the alumina regions around the crack-tip, which was attributed to microstructure inhomogeneities. The crack was further extended and the influence of the stress distribution within the alumina regions on the crack extension direction is briefly discussed.

R. J. Moon · M. Hoffman (✉)
School of Materials Science and Engineering,
The University of New South Wales, Sydney, NSW 2052,
Australia
e-mail: Mark.Hoffman@unsw.edu.au

S. Tochino · C. J. Lee · G. Pezzotti
Department of Materials, Ceramic Physics Laboratory,
Kyoto Institute of Technology, Sakyo-ku, Matsugasaki,
Kyoto 606-8585, Japan

Present Address:
R. J. Moon
Department of Agriculture, Forest Service: Forest Products
Laboratory, One Gifford Pinchot Drive, Madison,
WI 53726-2398, USA

Introduction

The fracture toughness and crack growth resistance of ceramic components can be increased by the inclusion of a ductile phase into the ceramic matrix, in which the reinforcement morphology can have a major influence [1–4]. One method of producing metal–ceramic composites is by metal infiltration of a porous ceramic preform [4, 5]. The resulting metal–ceramic composite has an interpenetrating network microstructure offering potentially improved fracture toughness, as compared to composites with a mono-dispersed metal phase in a ceramic matrix, because the crack cannot circumvent the metal phase during crack extension [1–3].

The method by which the ceramic preform is produced will strongly influence its pore structure, and thus influence the morphology of the infiltrated metallic phase within the composite. Porous ceramic bodies produced by partial sintering of ceramic powder will result in a porous structure on the same order as that of the ceramic grain size (<1–5 μm). An alternative method of producing porous ceramic preforms is by colloidal infiltration of an open-celled polymer foam [6]. After sintering, the resulting ceramic has an interconnecting pore structure that is similar to the ligament structure of the foam. During metal infiltration, the metal fills the pore structure and the resulting metal ligament size scale can be 10s to 100s of microns in diameter. Changes to the size scale and morphology of the metal-ceramic microstructure produced from the different processing techniques will alter the residual thermal stress distributions within each phase [7] and will modify the fracture behavior [4, 8].

Residual thermal stresses can develop in both the metal and ceramic phases as the infiltrated composite is cooled from the infiltration temperature to room temperature, since the two phases have different coefficients of thermal expansion [9, 10]. The magnitude of the thermal stresses that develop within metal–ceramic composites is dependent on the volume fraction of each phase [9], the strength of the interfacial bond between both phases, the temperature range over which stresses cannot be relieved via creep [9], the plastic deformation behavior of the metallic phase (ductility, yield stress, work hardening, creep, etc.) [7, 9] and the mechanical constraint experienced by the metal phase due to the surrounding ceramic phase [7, 10]. The plastic deformation behavior of metallic phases in metal–ceramic composites has been reported to be dependent on the metal ligament size (diameter) which affects the scale of mechanical constraint experienced by the metal phase [10, 11]. By decreasing the metal ligament diameter, mechanical constraint is increased, resulting in the metal ligaments withstanding a higher stress before yielding [7]. This suggests that the magnitude of thermal residual stress within the composite will then also increase.

The crack-tip stress fields in homogeneous composite materials are influenced by the stiffness, morphology, relative size scale of the microstructure and volume fraction of the constituent phases. The macroscopic crack-tip stress fields, where distances from the crack-tip are greater than the scale of the microstructure, will behave symmetrically about the crack-tip as in homogeneous materials. However, for a microscopic crack-tip stress field, the stress field will be highly influenced by asymmetrical microstructural constraints, leading to a stress field, which is not symmetrical about the crack-tip. This stress field asymmetry will influence the localized crack extension direction, creating a driving force for crack kinking. The stress distributions within composites has been an active field of research [12–16], however, the majority of the investigations have involved analytical and numerical modeling with no or limited experimental verification.

The ability to experimentally verify microstress distributions may offer new insights for improving existing theoretical modeling techniques, by confirming or disproving the factors which most effect crack-tip stress fields and the resulting crack extension path. The present study uses fluorescence microprobe spectroscopy to measure the residual thermal stress fields and crack-tip stress fields that develop in a ~30 vol% Al–70 vol% Al_2O_3 composite in which the metal ligament size is on the order of 10's of microns in diameter.

Sample preparation

Interpenetrating Al–Al_2O_3 composites were produced by liquid metal infiltration into ceramic preforms. A complete description of the infiltration technique used is given in [5, 6], but a brief description will be given here. The ceramic preforms were produced via colloidal infiltration of open-celled polyurethane foams (Bulpren S-31048, Eurofoam, Troisdorf, Germany). Initially, the foam had a relative density of 2.5% and a pore size of ~0.28 mm (corresponding to 90 pores per inch given by the manufacturer) and was compression molded to the desired relative density. The foam was then infiltrated with an alumina slip (25 vol% solids, 99.99% Al_2O_3, 0.4 μm average particle size, <1 ppm Cr, Taimicron TM-DAR, Taimei Chemicals Co. Ltd.) and dried. The resulting piece was fired in a two-step process to pyrolise the foam and then to sinter the ceramic. The porous alumina preforms were then infiltrated with aluminum using a pressure infiltration process that is outlined in [4, 5]. The final product was >99% of the theoretical density, in which the aluminum regions have the morphology resulting from the compressed foam ligament structure. While the polycrystalline alumina regions (~50–100 μm) have the morphology of the compressed foam pores as shown in Fig. 1. The alumina grain size within these regions has been observed in other studies to be <1 μm.

A composite tile having ~30 vol% Al–70 vol% Al_2O_3 was surface-ground flat using a 600 grit diamond wheel and multiple bend bars measuring 4 mm × 3 mm × 40 mm were then cut from the tile. The

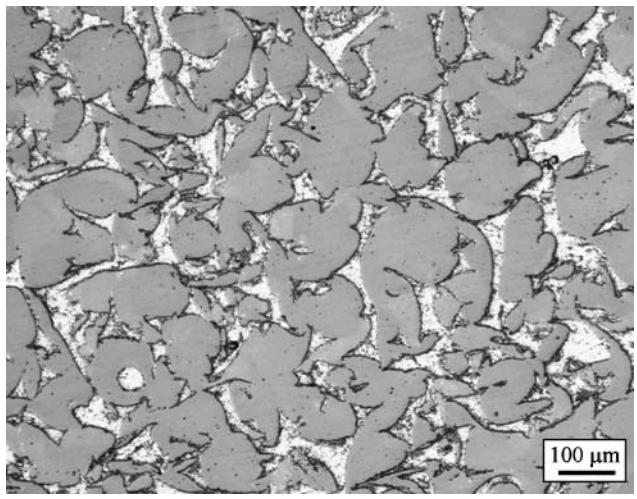

Fig. 1 Optical micrograph of the ~30 vol% Al–70 vol% Al_2O_3 composite showing the size scale and morphology of the aluminum and alumina regions. Note that the aluminum is the white colored phase and the alumina is the gray colored phase

4 mm × 40 mm side-surfaces were additionally polished to 1 μm diamond abrasives. A single edge V-notched beam (SEVNB) was produced by cutting a notch across the 3 mm × 40 mm face, perpendicular to the length of the bend bar, by first using a diamond cutter (0.2 mm blade thickness) and then a razor blade coated with fine diamond paste, which was used to sharpen the notch radius [17]. A crack was extended from the V-notch by loading the sample in a three-point bending load fixture (16 mm span width) in a screw driven mechanical testing machine with a displacement rate of 0.05 mm/min.

Experimental procedure

The fluorescence spectroscopy experimental procedure used in this study was similar to that previously described in [18], however, a brief description will also be given here. Fluorescence lines of Cr^{+3} substitutional impurities in alumina were collected at room temperature. The sample surface was irradiated with an Ar^{+} ion laser (wavelength of 488 nm, at 200 mW power, ~5 μm spot size) in which an optical microscope was used to both focus the laser on the sample surface and to collect its scattered radiation. The laser beam was focused on the sample surface, but due to the translucency of polycrystalline alumina the interaction volume of the laser light will encompass a region from the surface to several 10's of microns below the surface (~30 μm for polycrystalline 100 vol% alumina) and the resulting measured frequency is then an average over this volume [12]. It was assumed that the interaction volume of the laser light was constant for every point measured in the composite material. A triple monochromator (NR T64000, Jobin-Yvon/Horiba, Tokyo, Japan) equipped with a CCD detector was used to preform the analysis. A neon discharge lamp was used in all measured spectra as a frequency calibration standard.

Notched bend bars were loaded in a specialized three-point bend fixture (16 mm span width and equipped with a 100 N load cell) and placed onto the microscope stage of the Raman spectroscopic apparatus. An automatic traveling stage, having a 1 μm lateral displacement resolution, was used for directing the laser spot to the desired locations on the sample surface. An area ~250 μm square in the neighborhood of the crack-tip was selected, and the fluorescence spectra of this area were obtained by collecting individual spectra, each of 1 s acquisition time, over a 5 × 5 μm grid-like array of points within this selected area. All experiments were conducted in an isolated environmentally controlled room at 24 °C, in which temperature variations were less then 1 °C.

The fluorescence spectra were analyzed with curve-fitting algorithms included in the LabSpec software package (Horiba Co.) to estimate the R1 peak intensities and peak wavenumbers. Note that the neon standard spectra directly overlapped with the alumina R2 fluorescence peak, consequently the R2 peak was not used in the analysis. The R1 spectra wavenumber shifts were obtained from the difference between the peak centers of stressed (residual and/or externally applied stresses) and unstressed conditions. The hydrostatic stress within the alumina phase, σ, in the Al/Al_2O_3 composite was calculated by the shift in wavelength, ν, of the R1 alumina fluorescence spectra line, via the relation:

$$\langle \sigma \rangle = \frac{\Delta \nu}{\langle \Pi \rangle} \tag{1}$$

where $<\Pi>$ is the piezospectroscopic coefficient. For calculating the residual thermal stress field from sample processing and the crack-tip stress fields from the applied load, a three-dimensional R1 piezospectroscopic coefficient was used, where $<\Pi>_{3d} = \Pi_{11} + \Pi_{22} + \Pi_{33}$, with $\Pi_{11} = 2.56$ cm^{-1}/GPa, $\Pi_{22} = 3.5$ cm^{-1}/GPa and $\Pi_{33} = 1.53$ cm^{-1}/GPa [19]. A detailed description of the foundations of the stress analysis technique is given in [12]. Note that the R1 line frequency shifts along the *a*-axis in single crystal sapphire have been reported to be slightly non-linear [19], however, for polycrystalline alumina subjected to small changes in stress (~500 MPa) the deviations from linearity are within the scatter of the data [20].

The unstressed alumina R1 absolute wavenumber was estimated using a 3 vol% epoxy–97 vol% Al_2O_3 composite, which was produced identically to the method described in the sample preparation section, but the porous ceramic preform was infiltrated with epoxy (Epofix, Struers, Germany) [21] rather than with aluminum. Spectra were obtained under conditions as described earlier in this section, and the unstressed alumina R1 absolute wavenumber was obtained from averaging 2600 individual spectra that were taken over a 250 μm × 250 μm mapping area, in which the standard deviation was 0.013 (cm^{-1}). Note that minimal residual thermal stresses would be imparted by the epoxy on to the alumina due to the low epoxy volume fraction, the low modulus of the epoxy and the curing of the epoxy at room temperature. Additionally, the sintering stress distribution within the alumina phase was believed to be averaged out due to the large number of spectra taken, and due to the fact that the

interaction volume in which the fluorescence was measured was many times larger then the average alumina grain size (~1 μm). This averaging is partially supported by the small standard deviation of the measured R1 absolute wavenumber.

To investigate the residual thermal stress distribution resulting from sample processing, a fluorescence spectra map was collected with the sample having zero external applied load. The measured R1 absolute wavenumbers were compared to nominally unstressed alumina, and any shifts were then used in Eq. 1 to calculate the residual stress distribution.

The analysis of crack-tip stress fields is somewhat more involved. Fluorescence spectra maps were collected from the identical areas, with the sample having 0 N, 33 N and 50 N externally applied loads. The R1 spectra maps measured when the sample was subjected to an applied load, have components from both the pre-existing residual thermal stress and the external applied load. To remove the influence of the residual stress, the unloaded spectra map was subtracted from the loaded R1 spectra maps. The resulting shifts in the final R1 spectra represent the stresses that developed solely from the external load.

Results

Crack extension

A bend bar sample 2.93 mm × 3.45 mm × 41.0 mm, with an average V-notch depth of 1.61 mm, subjected to a critical applied load of 99 N initiated a ~0.42 mm long crack from the notch tip. The resulting fracture toughness of 6.4 Mpa.m^{½} was calculated from a standard three-point bending fracture equation [22]. With the large size scale of the microstructure the fracture path was tortuous, and it was common to see the crack kink ~50 μm as it attempted to circumvent the ductile aluminum regions. Along the length of the crack, several ductile aluminum regions bridged the crack. Figure 2a is an optical micrograph of the region around the crack-tip that was mapped, where the propagated crack can be seen in the middle of the image. The crack is not continuous and it appears to have kinked around the metal ligament region. The crack-tips of each crack segment can be seen to terminate at an Al–Al_2O_3 interface. Thus, to analyze the stress distribution around the crack-tip a relatively large area was mapped due to the uncertainties of the next crack extension location. It should be pointed out that the subsurface crack-front will be likewise disjointed and will not extend uniformly through the thickness of the sample.

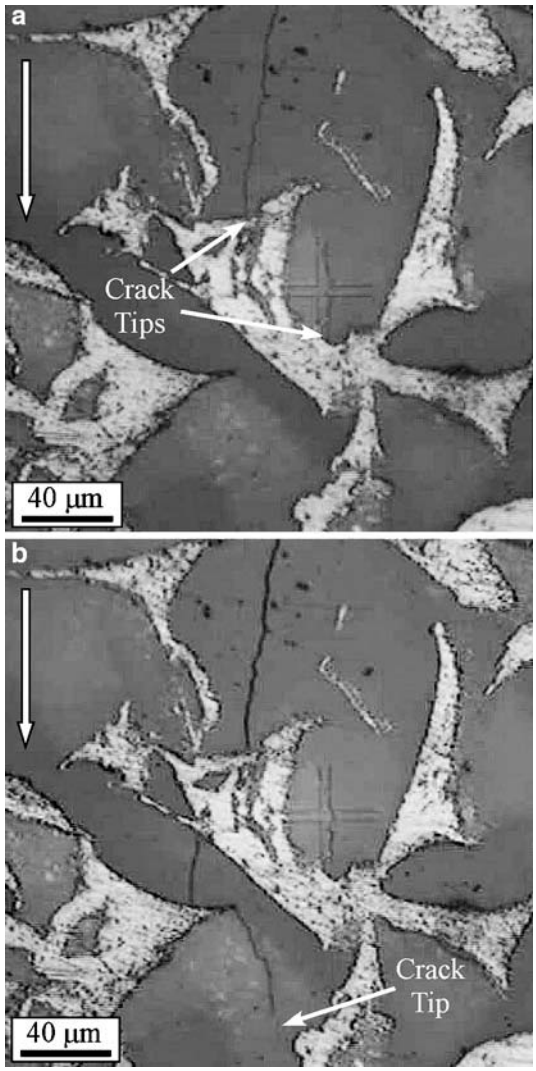

Fig. 2 Optical micrograph of the Al/Al_2O_3 composite showing the region around the crack-tip that was mapped for the (**a**) initial crack configuration, and (**b**) for the second crack configuration. The aluminum is the light colored phase, the alumina is the dark colored phase and the wide arrow points to the crack extension direction

Figure 2b is an optical micrograph of the region around the crack-tip after the crack was further extended (second crack extension). The crack is observed to circumvent the ductile aluminum region that was in front of the previous crack-tips. The calculated fracture toughness for the second crack extension was K = 7.2 Mpa.m^{½}, which is larger then that necessary to initiate the crack and thus demonstrates the presence of crack growth resistance behavior in this material [5].

Intensity distribution

The R1 alumina fluorescence-line-intensity distribution map of the first crack extension is shown in Fig. 3a. The

measured R1 intensity distribution maps were nearly identical for all mappings of this area, including after the second crack extension. In general, the R1 intensity distribution result is as expected; the aluminum regions, not having a fluorescence response at this wavelength, have low intensity and the alumina regions have high intensity. Some aluminum regions have a measured R1 alumina fluorescence line intensity which is believed to result from the ~5 μm spot size including a measurable amount of neighboring alumina. There was a large distribution in the R1 alumina fluorescence line intensity within the alumina regions, which does not appear to be directly related to the thickness of the alumina regions. The exact reasons for these intensity variations are unclear, but are believed to be partially associated with a changing alumina/aluminum ratio within the laser spot sampling volume.

The regions having intensities below 150 counts, the grey regions in Fig. 3b, were considered to have an increased likelihood of having the R1 wavelength influenced by the background noise of the system and in the subsequent figures these regions will be highlighted in white.

Residual thermal stress distribution

The residual stress distribution for the initial crack configuration is shown in Fig. 4, where it is seen that the alumina regions have a distribution of residual compressive stress of ~40–340 MPa. The alumina regions are expected to be on average in compression due to its lower thermal expansion coefficient relative to the aluminum phase. The distribution of stress within the alumina regions is believed to result from the local compositional and morphological inhomogeneities of both phases in this interpenetrating network microstructure (Fig. 2). This is consistent with the finite element modeling study by Agrawal et al. [23] of an idealized Al–Al_2O_3 co-continuous network structures, in which the thermal stress distribution in both phases was not uniform, and appeared to be influenced by phase boundaries, corners and localized structural variation.

The thermal stress distribution along the length of the crack would have been expected to be relieved due to the creation of free surfaces on the crack flanks. However, this was not observed. The fact that the thermal stress distribution about the crack appears to be unaffected by the crack suggests that the size of the fluorescence interaction volume is larger then the region of reduced stress along the crack surface. This is partially supported by the fact that the measured fluorescence intensity was not influenced by the presence

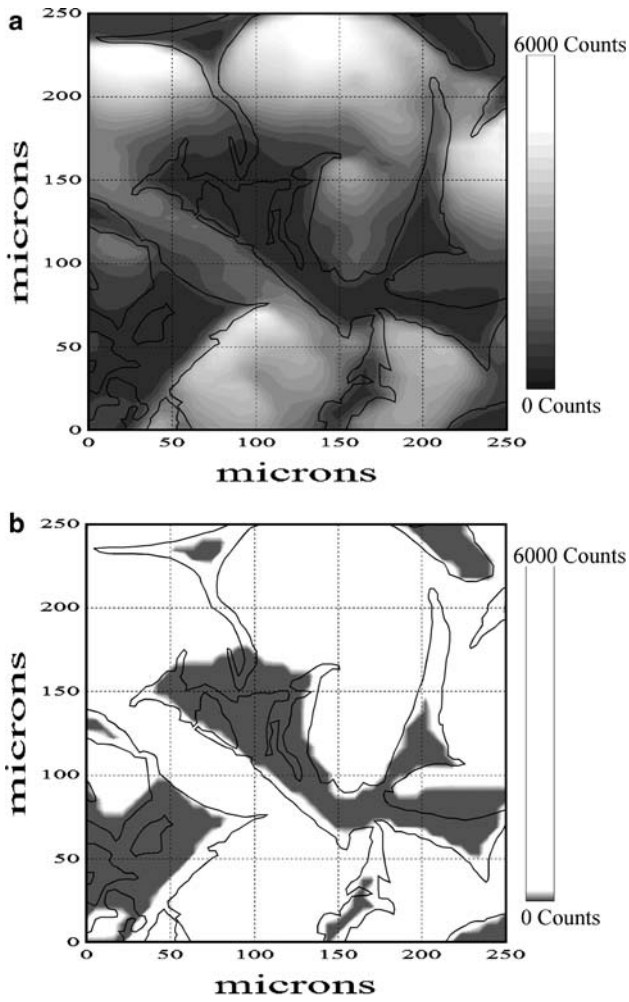

Fig. 3 The R1 alumina fluorescence-line intensity map with the outline of the microstructure overlaid. (**a**) Intensity map displaying the full range of intensities and (**b**) intensity map where regions having greater than 150 counts where colored white and regions having intensities less then 150 counts were colored grey

of the open space created between the crack surfaces, indicating that the measured interaction volume is large as compared to the crack opening.

External applied load stress distribution

The crack-tip stress distribution map resulting from the external applied load of 33 N for the initial crack configuration, shown in Fig. 5a, has an hydrostatic stress distribution in the alumina phase of 42 MPa compression to 109 MPa tension. In general, the stresses in the alumina regions are primarily tensile stresses of the order 0–40 MPa. By increasing the applied load from 33 N to 50 N it is seen in Fig. 5b that the stress distribution in the alumina became:

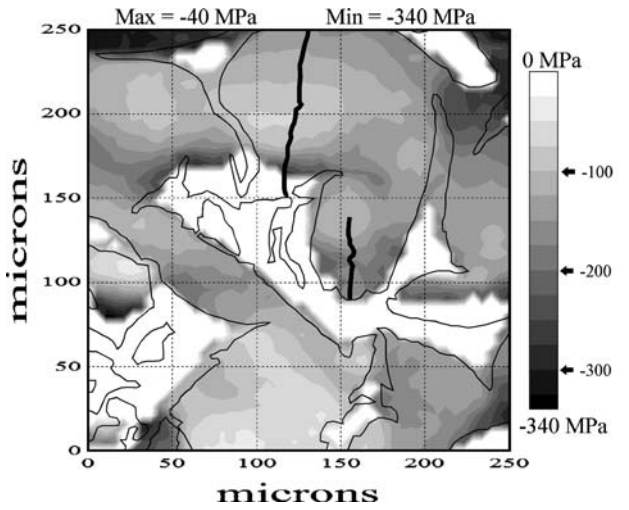

Fig. 4 The residual thermal stress distribution map, with the outline of the microstructure and crack (thick black line) overlaid. The areas that had measured intensities of less then 150 counts (Fig. 3b) were highlighted in white by artificially setting these regions to 0 MPa. The contours are in 25 MPa increments

17 MPa compression to 134 MPa tension. In general, higher tensile stresses within the alumina regions are seen; in particular the alumina regions in front of both crack-tips where the tensile stresses as high as ~100 MPa were measured. There is limited influence of the crack-tips in the stress distribution of the sample, which is to be expected because the crack-tips are located at the alumina/aluminum interfaces. However, it is observed that on either side of the crack there is a reduced amount of stress within the alumina, suggesting that the presence of the crack influence the resulting stress distribution within the alumina region.

The crack-tip stress distribution map resulting from the 33 N external applied load for the second crack configuration is shown in Fig. 6 and is similar to that of the first crack configuration resulting from the 33 N external load (Fig. 5a). The overall stress distribution was ~70 MPa compression to ~80 MPa tension. Interestingly, for the 33 N external applied loaded situations the stress in front of the crack appears to be lower then that at the crack-tip. This is believed to result the crack bridging of the aluminum ligaments behind the crack-tip resulting in appreciable crack-tip shielding of the applied load and results in stress distribution in the surrounding alumina phase around the bridging aluminum ligaments. For the 33 N external applied loaded it appears that most of the applied load is taken up by the crack bridging, and when the applied load is increased to 50 N the crack-tip begins to experience stress.

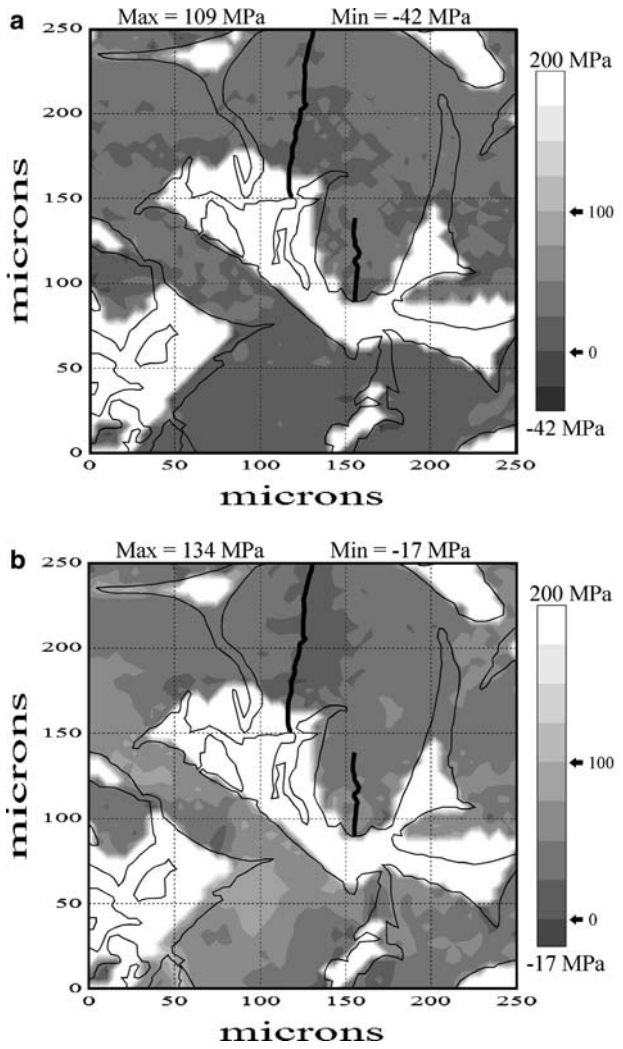

Fig. 5 Stress distribution map for the initial crack configuration, resulting solely from (**a**) 33 N and (**b**) 50 N external applied load, with the outline of the microstructure and crack (thick black line) overlaid. The areas that had measured intensities of less then 150 counts (Fig. 3b) were highlighted in white by artificially setting these regions to 200 MPa. The contours are in 25 MPa increments

Discussion

The ability of the fluorescence spectroscopy to measure the stress distribution about specific morphological features, along a crack length and at the crack-tip will be dependent on the relative size of the probe volume. For the current study the probe volume can be approximated by the 5 μm laser spot size combined with ~30 μm penetration distance into the subsurface, however, due to scattering the diameter of the probe volume will increase into the subsurface. The probe volume can be decreased by reducing the laser spot size and by using confocal techniques, neither of which was used in the current study. For the current study the

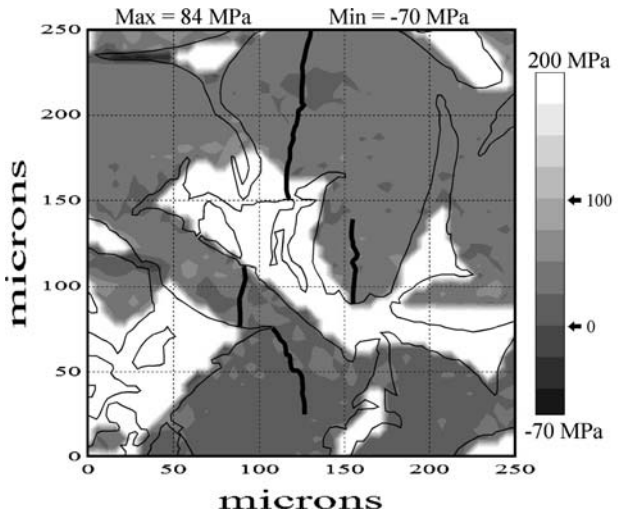

Fig. 6 Stress distribution maps resulting solely from the 33 N external applied load, with the outline of the microstructure and crack (thick black line) overlaid for the second crack configuration. The areas that had measured intensities of less then 150 counts (Fig. 3b) were highlighted in white by artificially setting these regions to 200 MPa. The contours are in 25 MPa increments

probe size was sufficiently small to measure the stress distribution within the 50–100 μm feature size. Note that the stress singularity directly at the crack-tip is difficult to measure; however, in the immediate region next to the crack-tip, ~20 μm, the near crack-tip stress is still very large and can be more easily measured with the probe volume used.

Residual thermal stress distribution

As demonstrated in Fig. 4, the alumina regions do not undergo a constant compressive stress loading from the thermal expansion mismatch between aluminum and alumina when the sample is cooled from the infiltration temperature. The observed distribution of stress is believed to result from the local compositional and morphological inhomogeneities of both phases in this interpenetrating network microstructure. The measured residual thermal compressive stress distribution within the alumina phase for a ~30 vol% Al–70 vol% Al_2O_3 composite was 40–340 MPa. The studies by Pezzotti and Sbaizero [18] and Hoffman et al. [7, 10] have also measured similar stress distributions within the alumina phase for ~30 vol% Al–70 vol% Al_2O_3 composites having interpenetrating network structures in which the metal ligaments were on the order of 1 μm. Pezzotti and Sbaizero [18], using fluorescence spectroscopy, measured a residual compressive stress distribution of 160 to 550 MPa. Likewise, Hoffman et al. [7, 10], using neutron diffraction and dilatometry, measured the residual thermal compressive stresses within the alumina phase of 50–400 MPa. This consistency in the measured stress within the ~30 vol% Al–70 vol% Al_2O_3 composites between the different investigations suggests that the magnitude of the stress as measured by the different techniques is realistic.

The stresses measured by Pezzotti and Sbaizero [18] and Hoffman et al. [7, 10] were larger and have a broader stress distribution than those of the current study. This is believed to result from the difference in the size of the metal ligament diameter and from the differences in the sharpness of the alumina phase morphology, which may concentrate stress within these features. The volume fraction of each phase was approximately the same between the different studies, but with the larger metal ligament diameter (10s of microns) in the current study, the mechanical constraint for plastic flow was much lower. Thus, there is a lower amount of stress necessary to cause plastic flow in the aluminum regions, which would result in a reduced residual compressive stress being imparted on the alumina regions. Additionally, the range of stress distribution may give an indication as to the variety of structural features within a phase morphology, in which for an alumina phase structure having sharper corners and recesses the localized effective phase fractions will be altered and result in localized higher and lower stresses. The finer phase morphology in the studies by Pezzotti and Sbaizero [18] and Hoffman et al. [7, 10] resulted in sharper corners and recesses, and thus increasing the thermal stress distribution as compared to the coarse alumina feature size of the current study.

Crack-tip stress distribution

The application of the 33 N and 50 N external load, for the sample and test geometry (assuming an elastically homogeneous material) and the initial crack length, would result in a crack-tip stress intensity factor of ~3.2 Mpa.$m^{½}$ and 4.9 Mpa.$m^{½}$, respectively. For the 30 vol% Al–70 vol% Al_2O_3 composite studied in this investigation the interconnecting network structure between the two phases will significantly alter the crack-tip stress fields, due to the presence of the phase boundaries and the differing stiffness of the two phases. The stress fields will be concentrated within the much stiffer alumina phase (Young's modulus: alumina ~390 GPa, aluminum ~70 GPa) and the three dimensional structure of the alumina regions will constrain the development of the stress fields around the crack-tip. During loading, additional stress fields will also be produced near the crack-tip region as the crack-tip stress fields interact with the stress concentrators

inherent in the alumina morphology (i.e., sharp corners, and recesses as seen in Fig. 1). Lastly, the transfer of crack bridging stress of the aluminum phase behind the crack-tip will also modify the stress within the alumina phase.

For the initial crack configuration, the crack-tip was located at an Al/Al_2O_3 interface and because of this the near crack-tip stress fields could not be measured. However, the far field stress fields within the alumina regions surrounding the crack-tip could be measured. As the applied load was increased from 33 N to 50 N, the stress distribution within the alumina regions changed. Figure 7 shows the resulting change in stress caused by the increase in the applied load, as calculated by subtracting Fig. 5a from Fig. 5b. The alumina regions behind the crack-tip did not change in tensile stress, but the alumina regions in the neighborhood of the crack-tip had increases in tensile stress in which the overall stress distribution surrounding the crack-tip region is not symmetrical. The largest increase of tensile stress of ~70 MPa, occurred in the alumina region in front of the crack-tips, region marked "I" in Fig. 7. Upon further crack extension the crack circumvented a ductile metal ligament and extended through the high tensile stress region, indicating that this local stress concentration influenced the crack extension direction.

The application of the 33 N external load for the second crack length resulted in a crack-tip stress

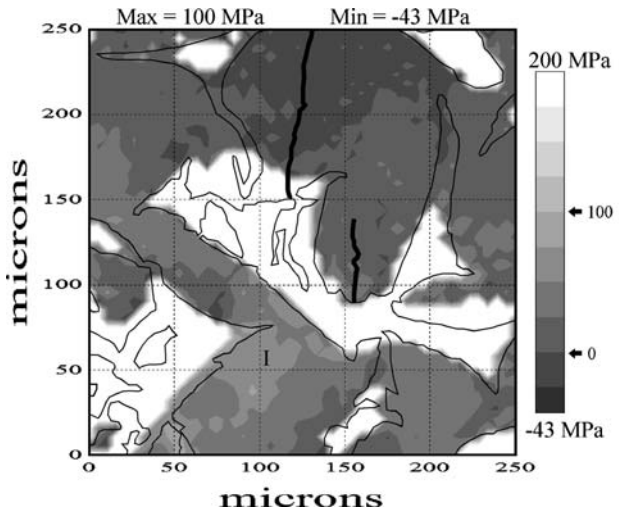

Fig. 7 The resulting change in the stress distribution, for the initial crack configuration, caused by increasing the applied load from 33 N to 50 N, calculated by subtracting Fig. 5a from Fig. 5b. The outline of the microstructure and crack (thick black line) are overlaid as a relative reference. The areas that had measured intensities of less then 150 counts (Fig. 3b) were highlighted in white by artificially setting these regions to 200 MPa. The contours are in 25 MPa increments

intensity factor of ~3.4 $Mpa.m^{½}$. With the crack-tip terminating within the alumina region (Fig. 2b), the near crack-tip stress fields could be measured, however, as shown in Fig. 6 the crack-tip stress fields are not apparent. One likely cause for this reduction of crack-tip stresses is the influence of crack bridging. The composite material tested in this study has a strong crack growth resistance behavior and it is likely, for the crack configuration shown in Fig. 2b, that the crack bridging by a large ductile metal ligament, ~50 μm behind the crack-tip, can partially shield the crack-tip from the applied stress and cause a reduction in the crack-tip stresses.

The results of the current study demonstrate that the stress distribution about the crack-tip within the brittle phase is influenced by the presence of the interpenetrating phase structure, and suggests fluorescence spectroscopy may be a viable technique to evaluate such stress distributions. The development of the asymmetrical stress profile within the brittle phase about the crack-tip region and the ability to be able to measures these stress distributions may provide insight as to the mechanisms, which dictate the resulting fracture behavior and fracture strength characteristics. The crack arresting and crack bridging capabilities of the more compliant phase has been considered dominant factors in controlling the fracture behavior of such composites. However, the development of the stress distribution within the less compliant brittle phase will also affect the crack initiation within that phase and the resulting crack propagation path, both of which are important factors in the composite fracture behavior.

Conclusions

Fluorescence microprobe spectroscopy was used to directly measure the stress distributions that develop within an interpenetrating 30 vol% Al–70 vol% Al_2O_3 composite resulting from the thermal expansion mismatch during sample processing, and those that develop near the crack-tip when the sample was subjected to an external load. The following conclusions can be drawn from this work.

(1) Fluorescence microprobe spectroscopy can be used to estimate the thermal stress and crack-tip stress distributions that develop within complex composite structures having feature size of 50–100 μm. The influence of the probe volume size and surface relaxation effects must be considered when quantitatively interpreting the results. This technique provides a method for visualizing the

resulting stress distribution and may assist in estimating the local crack extension paths.

(2) A distribution of residual thermal compressive stress developed within the alumina regions (~40–340 MPa), which was consistent with previous studies, but slightly lower in magnitude. It is suggested that the coarser metal ligament size in the current study decreased the confinement of the metal ligament, allowing for increased plastic flow and thus reducing the amount of residual stress within the alumina phase.

(3) The tensile stress distribution within the alumina regions surrounding the crack-tip were shown to increase (non-symmetrically) around the crack-tip by increasing the external load.

(4) Crack extension direction is influenced by the local crack-tip stress distributions and may be used to partially explain the tortuous crack path observed in this type of composites.

Acknowledgements The authors sincerely thank Prof. Jürgen Rödel of the Technische Universitaet Darmstadt, Germany for use of equipment and assistance during sample preparation. Additionally, the authors would like to thank Lyndal Rutgers of the University of New South Wales for providing the epoxy-alumina sample. This work was supported by the Australian Research Council, the Australian Academy of Science and the Japan Society for the Promotion of Science.

References

1. Venkateswara Rao KT, Soboyelo WO, Ritchie RO (1992) Metall Trans A 23A:2249
2. Badrinarayanan K, McKelvey AL, Venkateswara Rao KT, Ritchie RO (1996) Metall Trans A 27A:3781
3. Bloyer DR, Venkateswara Rao KT, Ritchie RO (1998) Metall Trans A 29A:2483
4. Prielipp H, Knechtel M, Claussen N, Streiffer S, Müllejans H, Rühle M, Rödel J (1995) Mater Sci Engng 197A:19
5. Neubrand A, Chung T-J, Rödel J, Steffler ED, Fett T (2002) J Mater Res 17(11):2912
6. Moon RJ, Tilbrook M, Hoffman M, Neubrand A (2005) J Am Ceramic Soc 88(3):666
7. Hoffman M, Skirl S, Pompe W, Rödel J (1999) Acta Mater 47:565
8. Hoffman M, Fiedler B, Emmel T, Prielipp H, Claussen N, Gross D, Rödel J (1997) Acta mater 45:3609
9. Skirl S, Hoffman M, Bowman K, Wiederhorn S, Rödel J (1998) Acta Mater 46:2493
10. Hoffman M, Rödel J, Skirl S, Zimmermann A, Fuller E, Mullejans H (1999) Key Eng Mater 159–160:311
11. Ashby MF, Blunt FJ, Bannister M (1989) Acta Metall 37:1847
12. Pezzotti G, Muller WH (2002) Continuum Mech Thermodyn 14:113
13. Wang C, Libardi W, Baldo JB (1998) Int J Fracture 94:177
14. Kassam ZHA, Zhang RJ, Wang Z (1995) Mat Sci Eng A203:286
15. Li Z, Chen Q (2003) Eng Frac Mech 70:581
16. Butcher RJ, Rousseau CE, Tippur HV (1999) Acta Mater 47(1):259
17. Kubler J (1997) Ceram Eng Sci Proc 18:155
18. Pezzotti G, Sbaizero O (2001) Mat Sci Eng A303:267
19. He J, Clarke DR (1995) J Am Ceram Soc 78:1347
20. Ma Q, Clarke DR (1993) J Am Ceram Soc 76:1433
21. Tilbrook M, Moon R, Hoffman M (2005) Mat Sci Eng A393:170
22. ASTM Standard E 1820-96 (1997) Standard test method for measurement of fracture toughness. ASTM, Philadelphia, Pa
23. Agrawal P, Conlon K, Bowman KJ, Sun CT, Chichocki FR Jr, Trumble KP (2003) Acta Mater 51:1143